ADVANCED MATERIALS
www.advmat.de

Transferrin Receptor-Targeted Nonspherical Microbubbles for Blood–Brain Barrier Sonopermeation

Anshuman Dasgupta, Tao Sun, Elena Rama, Alessandro Motta, Yongzhi Zhang, Chanikarn Power, Diana Moeckel, Stecia-Marie Fletcher, Mirjavad Moosavifar, Roman Barmin, Céline Porte, Eva Miriam Buhl, Céline Bastard, Roger M. Pallares, Fabian Kiessling, Nathan McDannold, Samir Mitragotri, and Twan Lammers**

Microbubbles (MB) are widely used for ultrasound (US) imaging and drug delivery. MB are typically spherically shaped, due to surface tension. When heated above their glass transition temperature, polymer-based MB can be mechanically stretched to obtain an anisotropic shape, endowing them with unique features for US-mediated blood–brain barrier (BBB) permeation. It is here shown that nonspherical MB can be surface-modified with BBB-specific targeting ligands, thereby promoting binding to and sonopermeation of blood vessels in the brain. Actively targeted rod-shaped MB are generated via 1D stretching of spherical poly(butyl cyanoacrylate) MB and via subsequently functionalizing their shell with antitransferrin receptor (TfR) antibodies. Using US and optical imaging, it is demonstrated that nonspherical anti-TfR-MB bind more efficiently to BBB endothelium than spherical anti-TfR-MB, both in vitro and in vivo. BBB-associated anisotropic MB produce stronger cavitation signals and markedly enhance BBB permeation and delivery of a model drug as compared to spherical BBB-targeted MB. These findings exemplify the potential of antibody-modified nonspherical MB for targeted and triggered drug delivery to the brain.

1. Introduction

Microbubbles (MB) are 1–10 µm sized air-filled vesicles shell-stabilized by lipids, proteins, or polymers.[1,2] Due to their large size, MB are confined within blood vessels and are unable to extravasate into tissues.[1–4] MB are routinely used in the clinic for ultrasound (US) imaging and drug delivery purposes. The mismatch in acoustic impedance between the MB gas core and surrounding tissue causes the MB to reflect US waves, thus providing contrast for functional and molecular US imaging.[3] For drug delivery, US-induced MB oscillation results in shear forces near vessel walls and cell membranes, thereby promoting vessel permeability and drug uptake.[4]

To improve MB-based ultrasound imaging and drug delivery, several design features, such as size, elasticity, shell composition and surface functionalization, have been explored over the years.[5–7] We recently added shape as a novel design parameter, demonstrating that nonspherical rod-like MB possess several unique features.[8] First, anisotropic MB were found to exhibit enhanced tumbling and margination, i.e., propensity to flow closer to blood vessel walls. Second, anisotropic MB showed reduced phagocytosis and circulated longer in the bloodstream of mice. Finally, anisotropic MB improved sonopermeation and delivery of a model drug across the blood–brain barrier (BBB).[8]

A. Dasgupta, E. Rama, A. Motta, D. Moeckel, M. Moosavifar, R. Barmin, C. Porte, R. M. Pallares, F. Kiessling, T. Lammers
Institute for Experimental Molecular Imaging
RWTH Aachen University Clinic
52074 Aachen, Germany
E-mail: tlammers@ukaachen.de

The ORCID identification number(s) for the author(s) of this article can be found under https://doi.org/10.1002/adma.202308150

DOI: 10.1002/adma.202308150

A. Dasgupta, T. Sun, S. Mitragotri
John A. Paulson School of Engineering and Applied Sciences
Harvard University
Boston, MA 02134, USA
E-mail: mitragotri@seas.harvard.edu

T. Sun, Y. Zhang, C. Power, S.-M. Fletcher, N. McDannold
Department of Radiology
Brigham and Women's Hospital
Harvard Medical School
Boston, MA 02115, USA

E. M. Buhl
Electron Microscopy Facility
Institute of Pathology
RWTH Aachen University
52074 Aachen, Germany

C. Bastard
DWI – Leibniz Institute for Interactive Materials
RWTH Aachen University Hospital
52074 Aachen, Germany

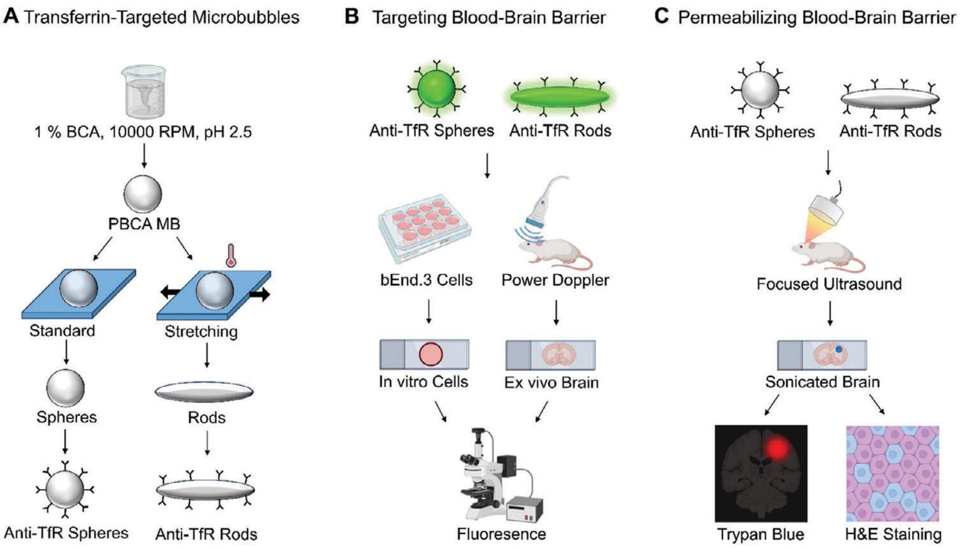

Figure 1. Study setup. A) Spherical MB were prepared by anionic polymerization of butyl cyanoacrylate (BCA) during vigorous stirring at 10 000 RPM at pH 2.5. Rod-shaped MB were generated by linearly stretching spherical MB in 1D at 70 °C and by subsequently cooling down the stretched MB to 25 °C. Targeted spherical and rod-shaped MB were prepared via controllably adsorbing anti-TfR antibodies to the shell of the MB. B) Fluorophore-labeled TfR-targeted spherical and rod-shaped MB were incubated with bEnd.3 cells in vitro and injected into healthy mice in vivo to study their binding to brain endothelium. C) TfR-targeted spherical and rod-shaped MB were i.v. administered in healthy mice and upon exposure to focused transcranial US, their ability to permeabilize the BBB and deliver a model drug to the brain was compared.

To further promote the unique features and functionalities of nonspherical MB, active targeting strategies can be considered, particularly surface functionalization with antibodies, peptides, or aptamers. This is attractive because anisotropic materials possess higher surface areas than spherical materials of equivalent volume, thereby providing more contact area for cell and blood vessel binding.[9,10] Taking this into account, we hypothesized that active targeting may help rod-shaped MB to bind more efficiently to blood vessels in the brain and to thereby enhance model drug delivery across the BBB upon treatment with transcranial focused US (FUS).

Accordingly, in the present study, we engineered vasculature-targeted anisotropic MB. Among antibodies, we purposely chose the high affinity antitransferrin receptor (TfR) antibody RI7217, which has demonstrated strong binding to brain vasculature in multiple mouse models,[11,12] to enable tight association with the vessel wall and to avoid dissociation under the high shear stresses experienced during blood flow and US-induced cavitation. Regarding MB composition, we chose a polymeric material, because this enables shape manipulation via temperature-induced transformation into a soft rubbery state, as well as shape retention upon cooling and transitioning back to a hard glassy state.[13,14] We specifically employed poly(butyl cyanoacrylate) (PBCA) MB, because these MB are well-characterized and widely used preclinically, and because PBCA is Food and Drug Administration-approved as a surgical adhesive for wound closure.[15]

Spherical PBCA MB were obtained upon anionic polymerization of butyl cyanoacrylate (BCA, **Figure** 1A). Rod-shaped PBCA MB were produced by linearly stretching spherical MB above their glass transition temperature (56 °C), followed by cooling down the stretched MB to room temperature.[16] Subsequently, anti-TfR antibodies (RI7217) were immobilized on the surface of the PBCA MB (Figure 1A).[9,17,18] We next labeled the MB with the fluorophore coumarin-6[19] and visualized and quantified the binding of anti-TfR spherical and anti-TfR nonspherical MB to brain endothelial cells in vitro and in vivo (Figure 1B). We finally intravenously (i.v.) coadministered anti-TfR spherical or anti-TfR nonspherical MB together with the non-BBB-permeable model drug trypan blue, and upon treating individual brain regions with transcranial focused US, we compared their ability to permeate and deliver trypan blue across the BBB (Figure 1C).

2. Results

2.1. Generation of Transferrin Receptor-Targeted Nonspherical Microbubbles

To obtain rod-shaped MB, spherical PBCA MB were embedded in a poly(vinyl alcohol) film, followed by 1D mechanical stretching of the film above the glass transition temperature of PBCA and subsequent cooling down to room temperature. Spherical and rod-shaped MB were then surface functionalized with anti-TfR antibodies as per previously established protocols.[9,17,18] The antibody-modified MB were characterized by assessing their shape, antibody density, size, and contact area. To this end, we first addressed the anisotropic shape of anti-TfR rod-shaped MB, via transmission electron microscopy and fluorescence imaging (**Figure** 2A,B). To validate MB surface functionalization with antibodies, fluorescein isothiocyanate (FITC)-labeled antibodies were used and their surface immobilization was quantified using a calibration curve derived from fluorescence spectroscopy (Figure S1, Supporting Information). We found an equivalent number of anti-TfR antibodies on the surface of both spherical and rod-shaped MB, with approximately 100 antibodies per individual MB in both cases (Figure 2C). The lengths of major axis, minor axis, aspect ratio, and actual surface area of anti-TfR

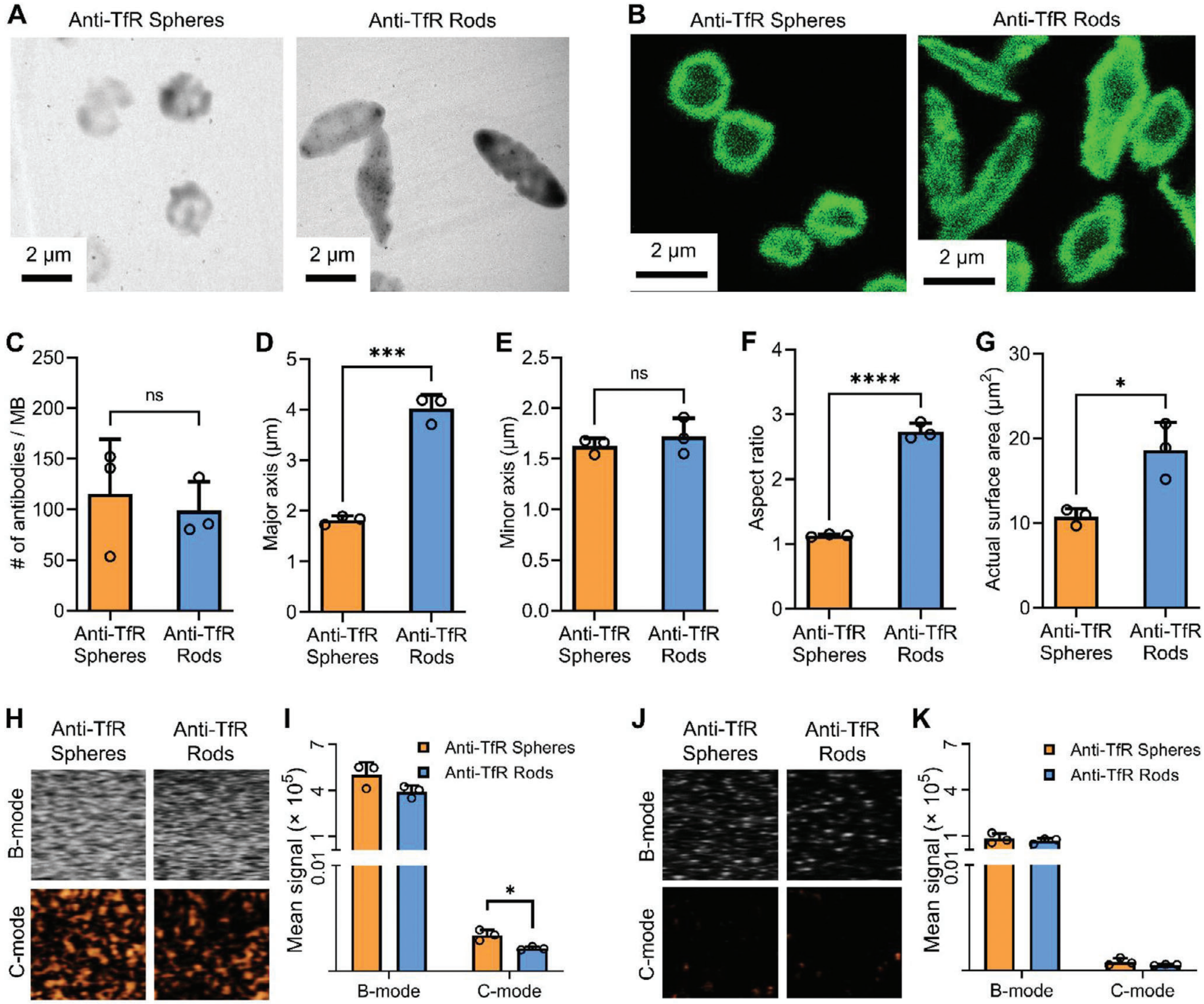

Figure 2. Generation and characterization of transferrin receptor-targeted nonspherical microbubbles. A) Transmission electron microscopy and B) fluorescence microscopy imaging confirms the anisotropic shape of anti-TfR-targeted rod-like MB. C–G) Analysis of physicochemical properties, showing that anti-TfR rod-shaped MB have a similar antibody density as spheres, while their major axis length, aspect ratio, and actual surface area is significantly higher. H,I) US imaging at 18 MHz center frequency and 0.03 mechanical index (MI) reveals that anti-TfR rod-shaped MB generated efficient B-mode and C-mode US signals, albeit somewhat lower than their spherical counterparts. J,K) Upon exposure to US at 18 MHz center frequency and 0.7 MI, B-mode and C-mode signals diminished, indicating efficient US-mediated destruction of both spherical and rod-shaped targeted MB. Data represent mean ± SD of three independent MB batches. In panels (D)–(G), each batch represents the mean of more than ten individual MB. Statistical comparisons were performed using unpaired *t*-test. *$p < 0.05$, ***$p < 0.001$, and ****$p < 0.0001$.

rod-shaped versus spherical MB were 4.0 ± 0.3 versus 1.8 ± 0.1 µm; 1.7 ± 0.2 versus 1.6 ± 0.1 µm; 2.7 ± 0.1 versus 1.1 ± 0.0; and 18.6 ± 3.3 versus 10.7 ± 1.0 µm^2, respectively (Figure 2D–G). The size distribution of anti-TfR targeted spherical and rod-shaped MB was found to be similar (Figure S2, Supporting Information).

Next, the US properties of antibody-targeted spherical and nonspherical MB were compared. To this end, 18 MHz center frequency was used at varying mechanical indexes (MI), as this frequency has previously been shown to generate strong US responses with PBCA MB.[8,15,19] At an MI of 0.03, anti-TfR-modified rod-shaped MB exhibited good brightness- and contrast-mode US signals (Figure 2H), although the intensities generated were slightly lower than those observed for their spherical counterparts (Figure 2I). Similar findings were observed at an MI of 0.07 (Figure S3A–C, Supporting Information). At a high MI of 0.7, analysis of initial time frames demonstrated very strong and transient US signals (Figure S4A–C, Supporting Information). However, at later time frames, there was hardly any detectable US signal, indicating that both spherical and rod-shaped anti-TfR MB were destroyed (Figure 2J,K). These findings illustrate that linearly stretching spherical PBCA MB above their glass transition temperature, followed by surface-functionalization with anti-TfR antibodies, results in the

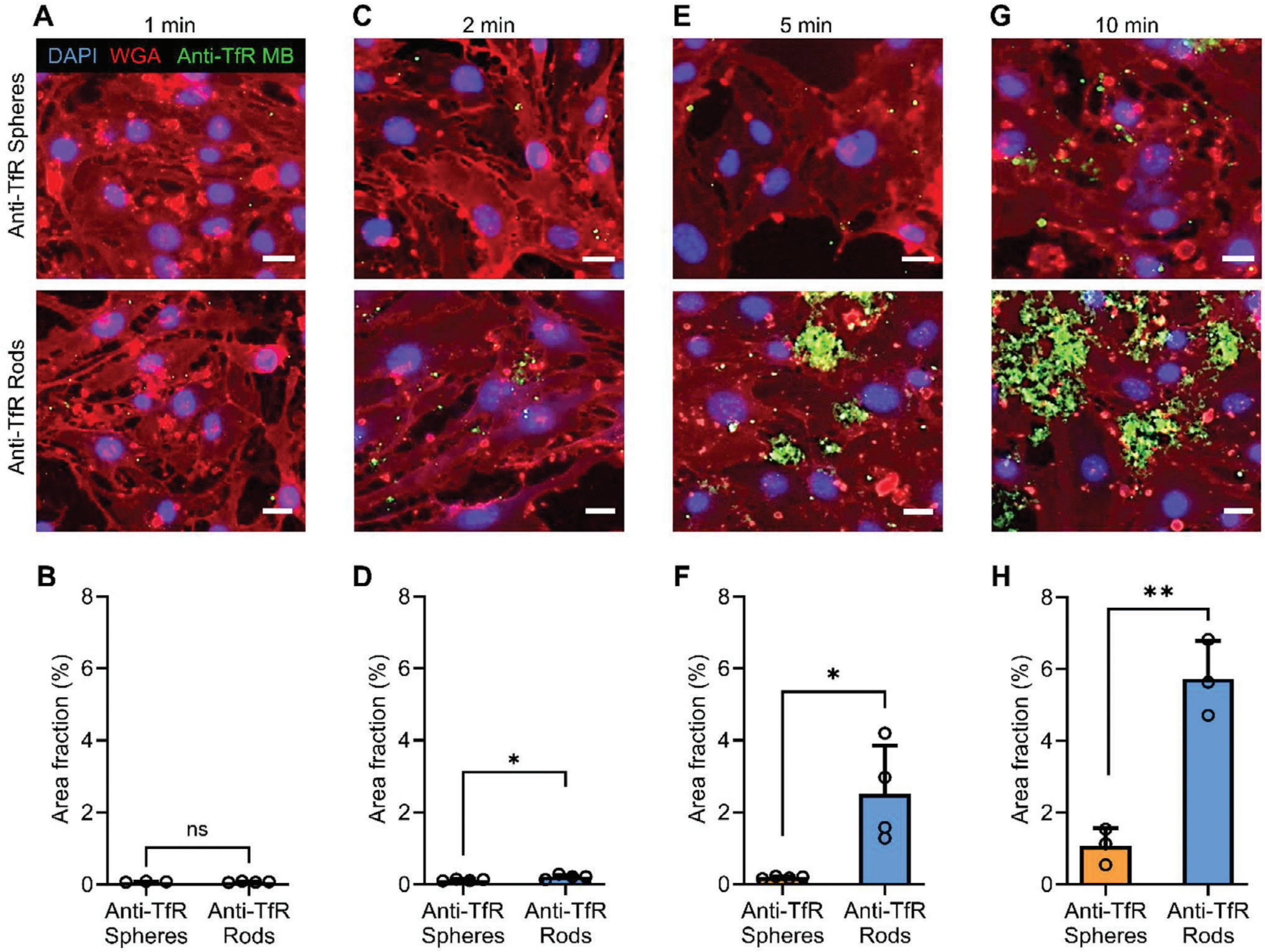

Figure 3. Transferrin receptor-targeted nonspherical microbubbles efficiently bind to brain endothelial cells in vitro. A–H) bEnd.3 mouse brain endothelial cells were incubated with spherical and rod-shaped coumarin-6-labeled anti-TfR MB, in order to study MB binding. A,B) At 1 min after the start of incubation, anti-TfR spherical and rod-shaped MB did not yet show strong signs of binding. C–H) At later time-points, anti-TfR-targeted rod-shaped MB demonstrated significantly greater binding to bEnd.3 cells than spherical anti-TfR MB. Cell nuclei were labeled with DAPI (blue), cell membranes with WGA (red) and MB with coumarin-6 (green). Scale bar is 20 µm. Data represent mean ± SD of three to four independent experiments. Statistical comparisons were performed using unpaired Student *t*-test. *$p < 0.05$ and **$p < 0.01$.

generation of stable and acoustically active rod-shaped MB, with ≈100 antibodies on their surface and with an aspect ratio of ≈2.5.

2.2. Transferrin Receptor-Targeted Nonspherical Microbubbles Bind to Brain Endothelial Cells In Vitro

To study the binding of TfR-antibody targeted MB rods and spheres to TfR-expressing cells, we employed bEnd.3 mouse-derived brain endothelial cells. Alike human brain endothelial cells, bEnd.3 cells express high levels of TfR.[20] Coumarin-6-labeled MB were used to assess their binding to bEnd.3 cells via fluorescence microscopy. We started off evaluating the specificity of anti-TfR MB for bEnd.3 cells by comparing their binding to control IgG isotype-modified MB. Anti-TfR spherical MB displayed slightly higher binding to the bEnd.3 cells versus IgG control spherical MB (Figure S5A,B, Supporting Information). For rod-shaped MB, their anti-TfR targeted counterparts demonstrated significantly higher binding to bEnd.3 cells than the IgG modified counterparts ($p < 0.01$; Figure S5C,D, Supporting Information).

Upon having confirmed the specificity of the anti-TfR antibody-targeted MB, we hypothesized that the increased contact area of rod-shaped MB will promote their binding to bEnd.3 cells in comparison to spherical MB. To evaluate this, bEnd.3 cells were incubated with anti-TfR spherical and rod-shaped MB under static conditions for different periods of time. At 1 min after initiating incubation, none of the two MB shapes produced strong fluorescent binding signals ($p > 0.05$; **Figure** 3A,B). After 2 and 5 min of incubation, TfR-targeted rod-shaped MB gradually started to show enhanced binding ($p < 0.05$; Figure 3C–F). At the intercellular level, we observed that for anti-TfR spheres, a large cell population did not show any signs of attached MB (Figure S6A, Supporting Information). In the case of anti-TfR rods, a relatively smaller fraction of the cells did not show any

MB binding. Moreover, a significant fraction of cells incubated with anti-TfR rods showed a very high number of MB bound to individual cells (i.e., more than 20 MB per cell; which was not observed for spherical MB; see Figure S6B, Supporting Information). At the last time point evaluated, i.e., 10 min post incubation, the difference in MB cell binding was clearly detectable, with anti-TfR rods showing a more than fivefold enhancement in attachment to bEnd.3 cells as compared to anti-TfR spheres ($p < 0.01$; Figure 3G,H). These results demonstrate that TfR-targeted nonspherical MB bind to endothelial cells more efficiently than TfR-targeted spherical MB under in vitro conditions.

2.3. Transferrin Receptor-Targeted Nonspherical Microbubbles Bind to Brain Endothelium In Vivo

We next evaluated if also under in vivo conditions, TfR-targeted rod-shaped MB bind more strongly to brain endothelial cells than their spherical TfR-targeted counterparts. We used US and fluorescence microscopy to monitor MB binding to brain endothelium. With regard to the former, we employed Power Doppler US imaging, as this enables the detection of moving MB, with a decrease in Power Doppler signal indicating either MB clearance or MB binding kinetics in real-time. We previously showed that rod-shaped MB clear less rapidly from the bloodstream than spherical MB;[8] consequently, the reduction observed in our current setup would correspond to active binding of MB to BBB endothelium. Furthermore, passive lodging of MB in the BBB will unlikely occur, as the MB are coated with a surfactant that is known to prevent lodging, and previous studies have not reported any signs of brain ischemia resulting from lodging and vessel occlusion.[5,8,21] In line with this, when i.v. administering anti-TfR antibody-modified MB and performing time-lapse Power Doppler US imaging, we indeed observed that the signal of anti-TfR rods decreased and disappeared faster than that of spherical anti-TfR MB (**Figure 4**A,B). Furthermore, at initial time points, i.e., at 1 and 2 min post injection, the Power Doppler US signal for anti-TfR rod-shaped MB was two to threefold lower than that of anti-TfR spherical MB ($p < 0.05$; Figure 4C). Similar findings were observed at later time points, i.e., at 3–5 min post injection, after which the Power Doppler US signal of anti-TfR rod-shaped MB disappeared ($p < 0.05$; Figure S7, Supporting Information).

After performing Power Doppler US analysis, ex vivo fluorescence imaging was performed to visualize and quantify anti-TfR MB binding to brain endothelium at the microscopic level. For this purpose, rhodamine-labeled lectin was injected i.v. prior to euthanizing the mice, in order to stain functional blood vessels. Whole brain tissue was then harvested and cryosectioned for ex vivo fluorescence microscopy. As shown in Figure 4D, we observed that TfR-targeted rod-shaped MB displayed noticeably higher signals in brain blood vessels than TfR-targeted spherical MB. We finally quantified both the percentage of MB found inside blood vessels (Figure 4E), and the intensity of their colocalization (Figure 4F), and observed that the amounts of TfR-targeted MB rods interacting with BBB endothelium were 2–3 two to threefold larger than those of TfR-targeted MB spheres ($p < 0.001$). Together, these results demonstrate that TfR-targeted nonspherical MB bind brain endothelial cells in vivo more efficiently than TfR-targeted spherical MB.

2.4. Transferrin Receptor-Targeted Nonspherical Microbubbles Potentiate BBB Sonopermeation

We finally assessed whether the enhanced binding of TfR-targeted rod-shaped MB results in an enhanced in vivo BBB permeation upon combination with FUS. For this purpose, anti-TfR MB were i.v. administered, followed by a lag-time of 10 min to enable nonbound MB to be cleared from the bloodstream, and to facilitate the binding of antibody-targeted MB to brain endothelium. After the 10 min gap, trypan blue was injected, serving as a non-BBB-permeable model, and then transcranial FUS was applied to bound MB for 5 min (**Figure 5**A). One hour after the end of FUS, mice were euthanized and brains were resected to study model drug delivery across the BBB (Figure 5A).

During transcranial FUS, passive cavitation detection monitoring was performed to record the acoustic emission signals of the spherical and nonspherical anti-TfR MB (Figure 5B). As a result of their enhanced binding to brain blood vessels, TfR-targeted rods produced threefold higher broadband cavitation signals than TfR-targeted spheres ($p < 0.05$; Figure 5C,D). The resulting broadband cavitation did cause a certain degree of brain damage in the sonicated area, as evidenced by erythrocyte extravasation and microhemorrhages (Figure S8, Supporting Information). To determine if this enhanced broadband cavitation of anti-TfR rod-shaped MB results in improved BBB permeation, trypan blue accumulation was analyzed in sonicated brain regions (Figure 5E). Upon harvesting brain tissue, we indeed observed that TfR-targeted rod-shaped MB markedly enhanced model drug delivery across the BBB as compared to their TfR-targeted spherical counterparts, increasing trypan blue accumulation in the focal US spot by more than a fourfold ($p < 0.05$; Figure 5F,G). In contrast to TfR-targeted MB rods, spherical anti-TfR MB hardly showed improvement in trypan blue delivery in the sonicated brain region when compared to its contralateral nonsonicated spot (indicated by dashed black line; Figure S9, Supporting Information). Grouping the obtained data sets, we lastly also assessed the relationship between the amount of trypan blue delivered and the measured broadband cavitation signals. As shown in Figure 5H, trypan blue delivery showed a stronger positive correlation with the cavitation signals for TfR-targeted rods ($r = 0.70$, $p = 0.09$) than for TfR-targeted spheres ($r = 0.55$, $p = 0.19$). Altogether, the transferrin receptor-targeted nonspherical MB developed in this study hold potential for actively targeting blood vessels in the brain and for promoting US-mediated drug delivery across the BBB.

3. Discussion

The combination of MB and US has been used to permeate the BBB, thereby enabling the extravasation and accumulation of drugs and drug delivery systems in the brain. This technique is commonly referred to as sonoporation or sonopermeation, and it is increasingly explored in clinical studies, in patients with brain cancer and beyond.[21–25] Several strategies have been employed

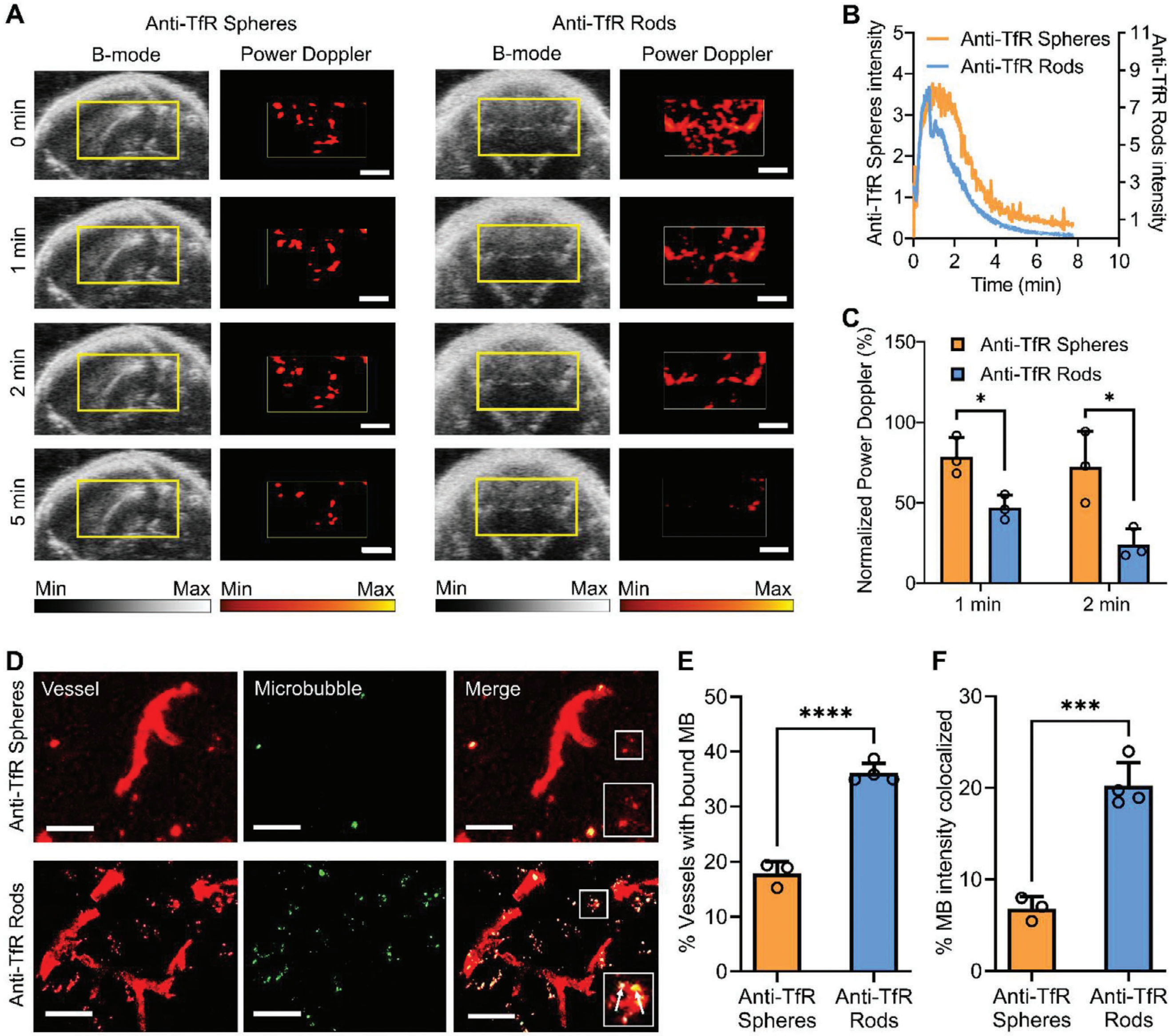

Figure 4. Transferrin receptor-targeted nonspherical microbubbles bind to brain endothelial cells in vivo. A) Time-lapsed B-mode and Power Doppler US imaging at a frequency of 18 MHz and MI of 0.07, indicating binding of anti-TfR rod-shaped MB to BBB endothelium. Yellow rectangular box highlights the corresponding region of interest imaged using Power Doppler US. Scale bar represents 1 mm. Color scales are similar for spheres and rods. B) Representative Power Doppler signal intensity over time curves for TfR-targeted spherical versus nonspherical MB. C) At 1 and 2 min post MB injection, the Power Doppler signal was significantly lower for anti-TfR rod-shaped MB than for anti-TfR spheres, indicative of more efficient binding to brain blood vessels. D–F) Ex vivo fluorescence microscopy imaging shows that more anti-TfR MB rods colocalized with blood vessels than anti-TfR spheres. The zoom images in the bottom right corners show that colocalization was also observed in small-sized blood vessels (highlighted with white arrows). Blood vessels and MB were labeled with rhodamine-lectin (red) and coumarin-6 (green), respectively. Scale bar is 50 µm. Data represent mean ± SD. Statistical comparisons were performed using unpaired *t*-test. $^{*}p < 0.05$, $^{***}p < 0.001$, and $^{****}p < 0.0001$.

to improve sonopermeation of the BBB. For instance, US parameters such as frequency, pressure, mechanical index, pulse, duration and others have been tailored to permeate the BBB in a safe and efficient manner.[26,27] In the case of MB, design features including size, size distribution, shell thickness, and shell composition have been optimized.[6,7,28,29] These efforts aim at controllably modulating the stable and inertial cavitation responses of MB, which are known to impact BBB permeability and drug delivery to the brain.[30,31]

We here changed the shape of MB and functionalized their surface with BBB-targeting antibodies for sonopermeation. Actively targeted nonspherical MB present unique attributes in both in vitro static and in vivo flow conditions. In case of former, the higher surface area available for interaction is the dominant feature of nonspherical MB. As a result, our findings show that actively targeted nonspherical MB bind much more efficiently to endothelial cells as compared to their spherical counterparts. We believe that upon FUS application, the enhanced

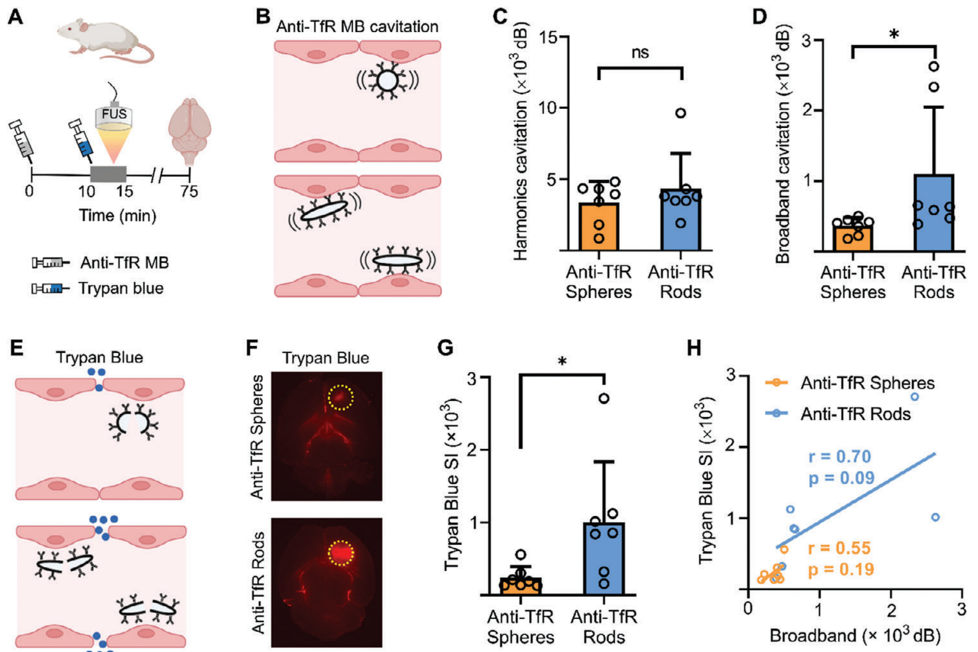

Figure 5. Transferrin receptor-targeted nonspherical microbubbles boost blood–brain barrier permeability upon focused ultrasound treatment. A) Schematic showing the BBB sonopermeation protocol employed. A total of 10^9 anti-TfR spherical and rod-shaped MB were i.v. administered to healthy mice, followed by a 10 min time-lag to enable MB binding and clearance from the bloodstream. Subsequently, trypan blue was i.v. injected as a non-BBB-permeable model drug and focused US was applied to permeate the BBB. Finally, brains were harvested to assess BBB permeation and drug delivery. B–D) A transducer with a resonant frequency of 278 KHz was used for FUS transmission. B) Sonication was performed transcranially at 835 KHz and the resulting cavitation signals of anti-TfR MB were recorded. Passive cavitation detection monitoring shows that anti-TfR MB rods produce C) similar harmonic and D) higher broadband emission signals as compared to anti-TfR MB spheres. E) The larger numbers and higher cavitation signals of TfR-targeted MB rods were hypothesized to improve BBB permeability and enhance model drug delivery. F,G) Ex vivo fluorescence imaging, exemplifying that anti-TfR-targeted rod-shaped MB enhance trypan blue delivery across the BBB upon transcranial FUS. Yellow-dashed circles represent the sonicated brain regions. H) Correlation of trypan blue delivery versus broadband cavitation signals, indicating a stronger positive correlation for TfR-targeted rod-shaped MB. Data represent mean ± SD (of $n = 7$ mice per group). Statistical comparisons for panels (C), (D), and (G) were performed using Student's *t*-tests. In panel (H), the data were analyzed using Pearson *r* correlation. $^*p < 0.05$.

retention of nonspherical MB will likely produce stronger cavitation signals, thereby improving drug delivery across cells under in vitro static conditions.[32,33] For in vivo flow setups, nonspherical MB will possess additional beneficial attributes, including higher surface area and enhanced margination and tumbling, i.e., intrinsic ability to travel closer to blood vessel walls.[8] These additional attributes will promote retention and contact time of nonspherical MB at the blood vessel wall, alike nonspherical nanoparticles.[9,10,17] Consequently, upon transcranial FUS application, antibody-modified brain vasculature-targeted nonspherical MB potentiated BBB sonopermeation and facilitated drug delivery (in)to the brain.

Following up on these encouraging findings, there is room for further improvement of our antibody-targeted nonspherical MB platform. First, the contact surface area of the MB can be further increased, to promote vascular binding even more. This can be achieved by engineering higher aspect ratio rods or by producing other anisotropically shaped MB, e.g., tetrahedrons or cubes, which naturally possess high surface area.[9,10] Second, the window between the harmonics and broadband emission signal can be improved, to achieve more safe and more efficient drug delivery. For this purpose, softer polymeric shell materials are needed, which at low acoustic pressures emit strong harmonic signals and negligible broadband signals.[34] Third, we here used a high affinity anti-TfR antibody, which induces irreversible binding. To ensure reversible binding between the antibody and the receptor, it will be important to evaluate MB surface-functionalized with lower affinity antibodies for targeting and permeabilizing the BBB.[11,35] Finally, our current production methodology may need some refinement, to enable robust scale-up production of antibody-coated nonspherical MB. This can be achieved by using hybrid sonication-microfluidic system containing multiple hydrodynamic flow-focusing orifices.[36,37]

Looking forward, we believe that actively targeted nonspherical MB hold potential for a range of different cell targeting and drug delivery approaches. They can also target endothelial cells and promote endothelium-specific drug delivery in organs other than brain. As an example, nonspherical MB can be functionalized with antibodies (or other targeting ligands) to enable binding to tumor vasculature, thereby, e.g., enhancing DNA or mRNA delivery transfection for production of immunogenic factors.[38,39] Other than endothelial cells, antibody-modified nonspherical MB can also target circulatory cells to prolong their circulation time and/or alter their biodistribution. Functionalizing nonspherical MB with anti-TER119 or anti-CD45 antibodies, for instance, may convey binding to erythrocytes for prolonged MB circulation, or to immune cells for MB targeting to sites of inflammation.[40,41] Taking everything together, antibody-functionalized nonspherical MB are considered to be promising new materials for targeting (intra)vascular cells and for promoting US-assisted drug delivery to the brain and beyond.

4. Conclusion

In summary, we engineered brain vasculature-targeted nonspherical MB by 1D stretching of spherical PBCA-based polymeric MB and by functionalizing their surface with anti-TfR antibodies. Compared to spherical TfR-targeted MB, rod-shaped TfR-targeted MB showed improved binding to brain endothelial cells in vitro and in vivo, and in combination with transcranial focused US, they markedly enhanced BBB opening and model drug accumulation in the brain. This indicates that actively targeted nonspherical MB are interesting materials for US-mediated drug delivery to the brain and beyond.

5. Experimental Section

Materials: BCA was purchased from Special Polymer Ltd (Bulgaria). Cold water soluble poly(vinyl alcohol) (PVA, 87–90% hydrolyzed, molecular weight 30 000–70 000 Da), coumarin, Triton X-100 and gelatin were bought from Sigma-Aldrich (Germany). Glycerol was bought from VWR. Purified and FITC-labeled anti-TfR antibody, clone RI7217, was purchased from BioLegend. IgG isotype control was procured from eBioscience. Trypan blue was obtained from Thermo Fisher Scientific. bEnd.3 cells were obtained from American Type Culture Collection (ATCC, Manassas, Virginia, USA). Deionized (DI) water was used for all experiments and all other reagents were of appropriate analytical grade.

Synthesis of Nonfunctionalized Spherical MB: PBCA-based spherical MB were synthesized using a previously established protocol.[19] Briefly, 3 mL of BCA monomer was added drop-wise to a 300 mL aqueous solution containing 1% (w/v) Triton X-100 at pH 2.5. Subsequently, the mixture was homogenized at 10 000 rpm for 1 h using an Ultraturrax (IKA-Werke, Germany). This led to the formation of nonfunctionalized spherical MB. Finally, the obtained spherical MB were washed multiple times at 500 rpm for 20 min and were finally suspended in 0.02% (w/v) Triton X-100 at pH 7.

Synthesis of Nonfunctionalized Rod-Shaped MB: Rod-shaped MB were synthesized using a previously established protocol.[8] Briefly, 15 g of cold water soluble PVA was dissolved in 80 mL of 0.02% w/v Triton X-100 at room temperature, followed by the addition of 1 mL of glycerol. 5 mL of nonfunctionalized spherical MB was next added to the mixture under constant stirring and later filtered through a 100 µm cell strainer to remove the aggregates. The mixture was then poured on a flat surface and allowed to dry for 48 h. The dried film were cut into 5×5 cm^2 and were mounted on a 1D stretcher and the system was placed in a paraffin oil bath at 70 °C for 10 min. Upon liquefaction, the films were stretched twofold in one-direction inside the oil bath at 70 °C. The films mounted on the stretcher was subsequently placed at room temperature for 30 min. The films were cleaned with kim wipes and isopropanol to remove the residual oil and were dissolved in 0.02% (w/v) Triton X-100 at room temperature to extract the MB. The resulting rod-shaped MB were allowed to float due to buoyancy, and the underneath aqueous solution was washed multiple times and were finally suspended in 0.02% (w/v) Triton X-100 at pH 7.

Synthesis of Antibody-Functionalized Spherical and Rod-Shaped MB: To prepare target specific MB, 10^{10} nonfunctionalized spherical and rod-shaped MB were incubated with 2×10^{14} anti-TfR antibodies at room temperature for 30 min. This enabled antibodies to be physically adsorbed on the MB surface.[9,17,18] The antibody-functionalized MB were placed at 4 °C and were allowed to float due to buoyancy. Subsequently, the underneath aqueous solution was washed to remove the unbound antibodies, and finally the anti-TfR spherical and rod-shaped MB were suspended in 0.02% (w/v) Triton X-100 at pH 7. Analogously, for generating untargeted counterparts, IgG isotype control were physically adsorbed on the surface of nonfunctionalized MB.

Synthesis of Coumarin-6 Labeled Antibody-Functionalized Spherical and Rod-Shaped MB: 50 mg of coumarin were dissolved in 1 mL dimethyl sulfoxide and was mixed with 20 mL of an aqueous suspension containing 10^{11} spherical MB. The reaction was allowed to proceed for 24 h at room temperature. After continuous mixing, MB were allowed to float due to buoyancy and the underneath aqueous solution was replaced multiple times to remove the unloaded coumarin. Finally, the coumarin-loaded spherical-shaped MB were suspended in 0.02% w/v Triton X-100 at pH 7 and stored at room temperature. To synthesize coumarin-loaded rod-shaped MB, coumarin-labeled spherical MB were manually stretched twofold in one-direction by employing the procedure as described above. Finally, the antibodies were attached on the MB surface using the above-mentioned protocol.

Beckmann Coulter Counter: The size distribution and concentration of targeted and untargeted spherical and rod-shaped MB were analyzed using a Multisizer 4 (Beckmann Coulter, Germany) which was equipped with a 30 µm sensor orifice.[19] Briefly, 20 mL of isotone solution was poured into a coulter counter cup and was placed on the sample platform. This was used as a blank measurement to correct for noise. Next, 10 µL of the MB were diluted with 20 mL of isotonic solution and the sample was measured in volumetric mode with a diltuion factor of 1000. These steps were repeated thrice to obtain mean ± standard deviation.

Bright-Field Microscopy: An Olympus BX41 microscope equipped with a microEye camera (Carl-Zeiss, Oberkochen, Germany) was used to validate the shape of anti-TfR spherical and rod-shaped MB. A drop of the MB sample was placed on a histobond adhesive microscope slide (Paul Marienfeld GmbH & Co.KG, Lauda-Königshofen, Germany). The images were acquired using Olympus 40x LMPlanFL N objective in bright-field mode. Image J software was employed to measure the MB size. For the major axis, the length was determined by calculating the longest diameter passing through the center and connecting the two vertices. The length of minor axis was calculated as the shortest possible line connecting the two covertices of the MB. The aspect ratio and the actual surface area of anti-TfR spherical and rod-shaped MB were calculated using the following mathematical equations

$$\text{Aspect ratio} = \frac{b}{a} \tag{1}$$

$$\text{Surface area of sphere} = 4\pi r^2 \tag{2}$$

$$\text{Surface area of rod} = 2\pi a^2 \left(1 + \frac{b}{ae}\sin^{-1} e\right) \tag{3}$$

where $e^2 = 1 - \frac{a^2}{b^2}$. The annotations b, a, r, and e represent semi-major axis, semi-minor-axis, radius, and eccentricity, respectively.

Confocal Laser Scanning Microscopy of Coumarin-6 Labeled Antibody-Functionalized Spherical and Rod-Shaped MB: The other method to confirm the anisotropic shape of the MB was via fluorescence microcopy. For this, a Leica TCS SP8 X inverted confocal microscope (Leica Microsystems, Wetzlar, Germany) was equipped with a plan-apochromat 93x/1.30 glycerol objective with a glycerol immersion liquid-type G (refractive index: 1.45). The samples were fixed with a drop of mowiol solution and applied on a high-precision cover glass. The samples were imaged with an excitation wavelength of 470 nm via a filtered white light laser, and the resulting emission was detected in the range of 491–556 nm. The images were analyzed via Leica Application Suite X Life Science Microscope software.

Transmission Electron Microscopy: For TEM (transmission electron microscopy) analysis, anti-TfR spherical and rod-shaped MB were adsorbed on glow discharged formvar-carbon-coated nickel grids (Maxtaform, 200 mesh, Plano, Wetzlar, Germany) for 10 min. Samples were examined using a Hitachi HT7800 TEM (Hitachi, Tokyo, Japan), operating at an acceleration voltage of 100 kV.

Quantification of Antibodies Functionalized on the MB Surface: To quantify antibody functionalization, FITC-labeled anti-TfR antibodies were physically adsorbed on the MB surface. 10 µL of anti-TfR spherical and rod-shaped MB were added to 90 µL of DI water. The fluorescence intensity from anti-TfR antibodies on the MB surface was determined using a TECAN Infinite M200 Pro device (Tecan Group Ltd, Germany). Subsequently, the concentration of attached anti-TfR antibodies was derived using a calibration curve, which correlated fluorescence intensity with the antibody concentration. The following parameters were used in the fluorescence spectroscopy: excitation wavelength: 480 nm, emission wavelength: 520 nm, excitation bandwidth: 9 nm, emission bandwidth: 20 nm, gain: 100, number of flashes: 25, integration time: 20 µs, lag time: 0 µs, settle time: 0 ms. Finally, the number of anti-TfR antibodies per MB was calculated as follows: (the concentration of the attached anti-TfR antibodies/molecular weight of the antibody) × Avogadro's constant/MB concentration.

US Imaging of Anti-TfR Spherical and Rod-Shaped MB: Preclinical US device (Vevo 3100, VisualSonics, Canada) was employed to visualize the contrast generated from anti-TfR spherical and rod-shaped MB.[42] Imaging experiments were performed using linear-array MX-250 transducer at 18 MHz center frequency. For sample preparations, 5×10^5 MB were diluted to 4.5 mL of 2% (w/v) gelation solution and the mixture was added into 10% (w/v) gelatin phantoms. The phantoms were imaged in both brightness-mode and nonlinear contrast mode at mechanical indices of 0.03, 0.07, and 0.7. A region-of-interest was drawn at the center of all images and the resulting contrast intensity was analyzed using the Vevo LAB software. The US imaging contrast of anti-TfR spherical- and rod-shaped MB were obtained from the contrast intensity generated at 0.03 and 0.07 MI. Finally, the percentage of MB destruction was quantified as: % MB destruction = ((contrast intensity at 0.03 MI – contrast intensity at 0.7 MI)/contrast intensity at 0.03 MI) × 100%.

Cell Culture: bEnd.3 mouse-derived brain endothelial cells were obtained from the ATCC (Manassas, Virginia, USA) and maintained in Dulbecco's Modified Eagle's Medium—1.5 g L^{-1} sodium bicarbonate with 10% fetal bovine serum and 1% penicillin. Cells were passaged every three to four days in T75 flasks. After the cells reached confluency, 1×10^5 bEnd.3 cells were seeded on gelatin-coated coverslips in a 24 well plate at 37 °C. Upon cell adherence to the coverslips and reaching 80% confluency, they were used to study the binding of anti-TfR spherical- and rod-shaped MB.

In Vitro Binding of TfR-Targeted Spherical- and Rod-Shaped MB to bEnd.3 cells: The adhered bEnd.3 cells were fixed with 4% paraformaldehyde for 10 min and washed with phosphate-buffered saline (PBS) at room temperature. To stain the cell membrane and nucleus, samples were incubated with wheat germ agglutinin (WGA, 1:500) Alexa Fluor 594 (Thermofisher Scientific, Massachusetts, USA) and 4',6-diamidino-2-phenylindole (DAPI, 1:500) (Thermofisher Scientific, Massachusetts, USA), respectively at room temperature for 30 min. Subsequently, 5×10^8 coumarin-labeled anti-TfR spherical and rod-shaped MB were incubated with bEnd.3 cells for 1, 2, 5, and 10 min at room temperature. For untargeted controls, coumarin-labeled IgG spherical and rod-shaped MB were incubated with bEnd.3 cells for 10 min. The samples were washed with PBS and the 12 mm round coverslips used as cell supports were removed from the 24 well plates using surgical tweezers. Finally, a drop of Mowiol mounting medium was placed on histobond adhesive microscope slide (Paul Marienfeld GmbH & Co.KG, Lauda-Königshofen, Germany) for adhering and attaching the coverslips.

Animal Experiments: All animal procedures were performed using protocols approved by the German State Office for Nature, Environment and Consumer Protection (Landesamt für Natur, Umwelt und Verbraucherschutz) North Rhine-Westphalia and by the Institutional Animal Care and Use Committee at Brigham and Women's Hospital. In these studies, injections were administered i.v. into the lateral tail vein unless stated otherwise.

Power Doppler Imaging: Vevo 3100 (VisualSonics, Canada) preclinical US device was used to visualize the Power-Doppler signal of MB over time in the brain. 6–8 weeks old female BALB/c nude mice were obtained from Janvier labs. Mice were randomly divided into two groups with five animals each. All injections and US imaging were performed on a temperature-controlled base to ensure maintenance of the animals body temperature (36.9 ± 1 °C) under inhalation anesthesia (induction with 4 vol% isoflurane with flow rate 1.8 L min^{-1} in oxygen-enriched air in induction chamber, maintenance of anesthesia with 2 vol% isoflurane with flow rate 1.2 L min^{-1} in oxygen-enriched air) using a dedicated vaporizer. Bepanthen ointment was used to protect the eyes from desiccation. Mouse brain was placed below the MS250 transducer at 18 MHz center frequency. Subsequently, 10^9 anti-TfR spherical or rod-shaped MB were coinjected with rhodamine lectin, and Power Doppler imaging was continuously employed for 10 min at an MI of 0.07. A region of interest was drawn within the brain and the resulting Power Doppler measurement was analyzed using a self-implemented Matlab (MathWorks, Natick, MA, USA) script. Broadly, this was done by determining the mean gray-level intensity of each Power-Doppler image after motion correction, resulting in a time-dependent signal curve. Finally, the mice were euthanized and the excised brains were preserved in optimal cutting temperature compound medium at −80 °C for further analysis.

Fluorescence Microscopy: To assess MB binding to bEnd.3 cells in vitro, multiple representative images per each sample were acquired using an Axio Imager M2 fluorescence microscope equipped with an AxioCam MRm Rev.3 camera (Carl Zeiss Microscopy GmbH, Oberkochen, Germany). These images were acquired at a magnification of 10x using the channels DsRed (for cell membrane), green fluorescent protein (GFP for coumarin-6 MB) and DAPI (for nucleus). To evaluate MB binding to the BBB in vivo, frozen brain tissue was cut in 10 µm slices using a cryotome (Cryostat CM3050 S, Leica Biosystems, Nussloch, Germany) and images were acquired using the DsRed (for vessels) and GFP (for coumarin-6 MB) channels. Next, all raw image files were imported to Fiji software (ImageJ, National Institues of Health) via BioFormat plugin. A custom macro script was utilized to automatically segment MB and vessels, maintaining consistent windowing and thresholding levels. Segmented masks and colocalization images were visually inspected by two independent users to confirm signal quality. Images with higher levels of noise or artefacts were excluded from the quantification. Finally, successful binding was quantified and defined as the area fraction of colocalized signals between different channels. In addition, also the signal intensity of colocalized areas was taken into account.

FUS-Mediated BBB Permeation: 6–8 weeks old BALB/c mice were anesthetized by i.p. injections of ketamine (80 mL kg^{-1} h^{-1}) and xylazine (10 mL kg^{-1} h^{-1}). After anesthesia, the fur on the head was removed using clippers and depilatory cream for efficient US propagation. The head was fixed in an acrylic stereotactic frame, and then the mouse was placed on the FUS device.

Mice were randomly divided into two groups with seven mice each. The first group received anti-TfR spherical MB and the second one was administered with anti-TfR rod-shaped MB. Based on the previous study, 0.91 and 1.29 MPa were chosen as the inertial cavitation thresholds for anti-TfR spherical and rod-shaped MB, respectively.[8] This ensured that a single anti-TfR spherical and rod-shaped MB produced similar levels of cavitation emission in vivo. For FUS-induced BBB opening, mice first received a dose of 10^9 MB, followed by a gap of 10 min. Immediately after the gap, trypan blue was injected and FUS was applied to induce BBB permeation. Sonications were performed using 10 ms bursts at 4 Hz for 100 s. FUS was applied on four targets centered in the brain striatum to permeabilize the BBB. An in-house FUS system was used for cavitation-controlled transmission. The transducer was spherically curved and made of lead zirconate titanate (diameter/radius of curvature: 10/8 cm) with a resonant frequency of 278 kHz. Transcranial sonications were applied at 835 kHz, i.e., the third harmonic of the transducer, to decrease the focal spot in small animal experiments. The transducer was mounted on a plastic plate which was attached to a manually operated, three-axis positioning system. The transducer was driven by a function generator (33220A, Agilent, Santa Clara, CA, USA) and an amplifier (240L, E&I, Rochester, NY, USA). Electrical power output was measured using a power meter (E4419B, Agilent, Santa Clara, CA, USA) and a dual-directional coupler (C5948-10, Werlatone, Patterson, NY, USA). The calibration of the transducers was performed using scans of the focal plane acquired with a needle hydrophone (HNC-1000; Onda, Sunnyvale, CA) and radiation force balance measurements, to estimate the pressure amplitude at the focal spot in water. The width and length of the 50% isopressure contours were 1.9 and 11.4 mm, respectively.

Passive cavitation detection recordings were performed using detectors with a resonant frequency of 650 kHz. The window for calculating broadband noise was also centered around 650 KHz, for high sensitivity (the whole window length is 20000 samples, with a sampling frequency of 10 MHz). The cavitation signal was recorded using a 12-bit high-speed digitizing card (PCX-5124, National Instruments, Austin, TX, USA). The time signal, frequency spectrum, and the tracked harmonic and wideband emissions were monitored and controlled in real time using in-house developed software in MATLAB (MathWorks, Natick, MA, USA).

Trypan Blue Brain Accumulation: BBB permeation was evaluated by assessing the accumulation of trypan blue in the brain. To this end, transcardiac perfusion was performed after the FUS treatment and subsequently the brains were harvested. The excised brains were fixed with 4% paraformaldehyde. Upon fixation, the brains were sectioned in a serial manner from the dorsal surface to the ventral surface with a thickness of 1 mm. The images of the brain sections were acquired using a fluorescence stereo zoom microscope (ZEISS Axio Zoom.V16, Carl Zeiss AG, Oberkochen, Germany). Finally, trypan blue accumulation across the BBB was quantified by measuring the total fluorescence intensity of all the brain sections.

Statistical Analysis: Data are represented as mean ± standard deviation. All results were analyzed using GraphPad Prism 9.1.1. Statistical analysis was performed using student unpaired *t*-test, unpaired *t*-test for multiple groups by the two-stage step-up method (Benjamini, Krieger, and Yekutieli), or using pearson *r* correlation as indicated in the Figure legends. Significance was determined at the following cutoff points: * $p < 0.05$, ** $p < 0.01$, *** $p < 0.001$ and **** $p < 0.0001$.

Supporting Information

Supporting Information is available from the Wiley Online Library or from the author.

Acknowledgements

T.L. acknowledges support by the European Commission (EuroNanoMed-III: NSC4DIPG), the European Research Council (ERC-CoG 864121: Meta-Targeting), and the German Research Foundation (DFG: GRK/RTG2375 (grant #331065168), SFB1066, and LA2937/4-1). S.M. acknowledges support from the John A. Paulson School of Engineering and Applied Sciences at Harvard University. N.M. acknowledges support from the National Institutes of Health (R01 EB033307). BioRender software (https://biorender.com) was employed for creating schematics. [Correction added on March 19, 2024, after first online publication: Projekt Deal funding statement has been added.]

Open access funding enabled and organized by Projekt DEAL.

Conflict of Interest

The authors declare no conflict of interest.

Author Contributions

A.D., S.M., and T.L. conceived and coordinated the study. A.D. performed experiments and analyzed results. M.M., R.B., E.M.B., C.B., R.M.P., and F.K. assisted with MB characterization. E.R., A.M., and S.M.F. helped with fluorescence microscopy. Ce.P. helped with Matlab programming. T.S., Y.Z., Ch.P., D.M., and N.M. assisted with the animal experiments. A.D. drafted the first version of the manuscript. S.M. and T.L. ciritcally revised, corrected and commented on the manuscript. All authors read and approved the final version of the manuscript.

Data Availability Statement

The data that support the findings of this study are available from the corresponding author upon reasonable request.

Keywords

anisotropy, blood–brain barrier, drug delivery, microbubbles, PBCA, ultrasound, vascular targeting

Received: August 11, 2023
Revised: October 19, 2023
Published online: November 27, 2023

[1] E. Stride, T. Segers, G. Lajoinie, S. Cherkaoui, T. Bettinger, M. Versluis, M. Borden, *Ultrasound Med. Biol.* **2020**, *46*, 1326.
[2] F. Kiessling, S. Fokong, P. Koczera, W. Lederle, T. Lammers, *J. Nucl. Med.* **2012**, *53*, 345.
[3] G. Köse, M. Darguzyte, F. Kiessling, *Nanomaterials* **2020**, *10*, 1935.
[4] J. Deprez, G. Lajoinie, Y. Engelen, S. C. De Smedt, I. Lentacker, *Adv. Drug Delivery Rev.* **2021**, *172*, 9.
[5] J.-N. May, S. K. Golombek, M. Baues, A. Dasgupta, N. Drude, A. Rix, D. Rommel, S. Von Stillfried, L. Appold, R. Pola, M. Pechar, L. Van Bloois, G. Storm, A. J. C. Kuehne, F. Gremse, B. Theek, F. Kiessling, T. Lammers, *Theranostics* **2020**, *10*, 1948.
[6] S. K. Wu, P. C. Chu, W. Y. Chai, S. T. Kang, C. H. Tsai, C. H. Fan, C. K. Yeh, H. L. Liu, *Sci. Rep.* **2017**, *7*, 46689.
[7] S.-Y. Wu, C. C. Chen, Y.-S. Tung, O. O. Olumolade, E. E. Konofagou, *J. Controlled Release* **2015**, *212*, 30.
[8] A. Dasgupta, T. Sun, R. Palomba, E. Rama, Y. Zhang, C. Power, D. Moeckel, M. Liu, A. Sarode, M. Weiler, A. Motta, C. Porte, Z. Magnuska, A. Said Elshafei, R. Barmin, A. Graham, A. Mcclelland, D. Rommel, E. Stickeler, F. Kiessling, R. M. Pallares, L. De Laporte, P. Decuzzi, N. Mcdannold, S. Mitragotri, T. Lammers, *Proc. Natl. Acad. Sci. USA* **2023**, *120*, 2218847120.
[9] P. Kolhar, A. C. Anselmo, V. Gupta, K. Pant, B. Prabhakarpandian, E. Ruoslahti, S. Mitragotri, *Proc. Natl. Acad. Sci. USA* **2013**, *110*, 10753.
[10] M. Cooley, A. Sarode, M. Hoore, D. A. Fedosov, S. Mitragotri, A. Sen Gupta, *Nanoscale* **2018**, *10*, 15350.
[11] I. Van Rooy, E. Mastrobattista, G. Storm, W. E. Hennink, R. M. Schiffelers, *J. Controlled Release* **2011**, *150*, 30.
[12] K. Kucharz, K. Kristensen, K. B. Johnsen, M. A. Lund, M. Lønstrup, T. Moos, T. L. Andresen, M. J. Lauritzen, *Nat. Commun.* **2021**, *12*, 4121.
[13] N. Kapate, J. R. Clegg, S. Mitragotri, *Adv. Drug Delivery Rev.* **2021**, *177*, 113807.
[14] J. A. Champion, Y. K. Katare, S. Mitragotri, *Proc. Natl. Acad. Sci. USA* **2007**, *104*, 11901.
[15] P. Koczera, L. Appold, Y. Shi, M. Liu, A. Dasgupta, V. Pathak, T. Ojha, S. Fokong, Z. Wu, M. Van Zandvoort, O. Iranzo, A. J. C. Kuehne, A. Pich, F. Kiessling, T. Lammers, *J. Controlled Release* **2017**, *259*, 128.
[16] R. K. Kulkarni, H. J. Porter, F. Leonard, *J. Appl. Polym. Sci.* **1973**, *17*, 3509.
[17] S. Barua, J.-W. Yoo, P. Kolhar, A. Wakankar, Y. R. Gokarn, S. Mitragotri, *Proc. Natl. Acad. Sci. USA* **2013**, *110*, 3270.
[18] M. Tonigold, J. Simon, D. Estupiñán, M. Kokkinopoulou, J. Reinholz, U. Kintzel, A. Kaltbeitzel, P. Renz, M. P. Domogalla, K. Steinbrink, I. Lieberwirth, D. Crespy, K. Landfester, V. Mailänder, *Nat. Nanotechnol.* **2018**, *13*, 862.
[19] M. Liu, A. Dasgupta, P. Koczera, S. Schipper, D. Rommel, Y. Shi, F. Kiessling, T. Lammers, *Mol. Pharmaceutics* **2020**, *17*, 2840.
[20] Y. Zhang, J. He, L. Shen, T. Wang, J. Yang, Y. Li, Y. Wang, D. Quan, *J. Controlled Release* **2021**, *329*, 1117.

[21] A. J. Calderón, Y. S. Heo, D. Huh, N. Futai, S. Takayama, J. B. Fowlkes, J. L. Bull, *Appl. Phys. Lett.* **2006**, *89*.
[22] A. Dasgupta, M. Liu, T. Ojha, G. Storm, F. Kiessling, T. Lammers, *Drug Discovery Today: Technol.* **2016**, *20*, 41.
[23] S. Snipstad, K. Vikedal, M. Maardalen, A. Kurbatskaya, E. Sulheim, C. D. L. Davies, *Adv. Drug Delivery Rev.* **2021**, *177*, 113847.
[24] P. Anastasiadis, D. Gandhi, Y. Guo, A.-K. Ahmed, S. M. Bentzen, C. Arvanitis, G. F. Woodworth, *Proc. Natl. Acad. Sci. USA* **2021**, *118*, 2103280118.
[25] A. Abrahao, Y. Meng, M. Llinas, Y. Huang, C. Hamani, T. Mainprize, I. Aubert, C. Heyn, S. E. Black, K. Hynynen, N. Lipsman, L. Zinman, *Nat. Commun.* **2019**, *10*, 4373.
[26] M. Aryal, C. D. Arvanitis, P. M. Alexander, N. Mcdannold, *Adv. Drug Delivery Rev.* **2014**, *72*, 94.
[27] S. Snipstad, E. Sulheim, C. De Lange Davies, C. Moonen, G. Storm, F. Kiessling, R. Schmid, T. Lammers, *Expert Opin. Drug Delivery* **2018**, *15*, 1249.
[28] K. H. Song, A. C. Fan, J. J. Hinkle, J. Newman, M. A. Borden, B. K. Harvey, *Theranostics* **2017**, *7*, 144.
[29] T. Sun, A. Dasgupta, Z. Zhao, M. Nurunnabi, S. Mitragotri, *Adv. Drug Delivery Rev.* **2020**, *158*, 36.
[30] E. Stride, C. Coussios, *Nat. Rev. Phys.* **2019**, *1*, 495.
[31] A.-H. Liao, C.-H. Wang, P.-Y. Weng, Y.-C. Lin, H. Wang, H.-K. Chen, H.-L. Liu, H.-C. Chuang, C.-P. Shih, *JCI Insight* **2020**, *5*.
[32] K. Kooiman, M. Foppen-Harteveld, A. F. W. V. Der Steen, N. De Jong, *J. Controlled Release* **2011**, *154*, 35.
[33] I. Beekers, S. A. G. Langeveld, B. Meijlink, A. F. W. Van Der Steen, N. De Jong, M. D. Verweij, K. Kooiman, *J. Controlled Release* **2022**, *347*, 460.
[34] A. Jafari Sojahrood, A. C. De Leon, R. Lee, M. Cooley, E. C. Abenojar, M. C. Kolios, A. A. Exner, *ACS Nano* **2021**, *15*, 4901.
[35] K. B. Johnsen, M. Bak, P. J. Kempen, F. Melander, A. Burkhart, M. S. Thomsen, M. S. Nielsen, T. Moos, T. L. Andresen, *Theranostics* **2018**, *8*, 3416.
[36] M. R. Kendall, D. Bardin, R. Shih, P. A. Dayton, A. P. Lee, *Bubble Sci., Eng., Technol.* **2012**, *4*, 12.
[37] D. Carugo, R. J. Browning, I. Iranmanesh, W. Messaoudi, P. Rademeyer, E. Stride, *J. Acoust. Soc. Am.* **2021**, *150*, 1577.
[38] J. K. Hennigs, C. Matuszcak, M. Trepel, J. Körbelin, *Cells* **2021**, *10*, 2712.
[39] V. Pathak, T. Nolte, E. Rama, A. Rix, S. M. Dadfar, V. Paefgen, S. Banala, E. M. Buhl, M. Weiler, V. Schulz, T. Lammers, F. Kiessling, *Biomaterials* **2021**, *275*, 120896.
[40] A. R. Crow, R. Kapur, S. Koernig, I. K. Campbell, C.-C. Jen, P. J. Mott, D. Marjoram, R. Khan, M. Kim, J. Brasseit, Y. Cruz-Leal, A. Amash, S. Kahlon, I. Yougbare, H. Ni, A. W. Zuercher, F. Käsermann, J. W. Semple, A. H. Lazarus, *Sci. Transl. Med.* **2019**, *11*, eaau8217.
[41] N. K. Lee, S.-N. Kim, C. G. Park, *Biomater. Res.* **2021**, *25*, 44.
[42] R. A. Barmin, A. Dasgupta, C. Bastard, L. De Laporte, S. Rütten, M. Weiler, F. Kiessling, T. Lammers, R. M. Pallares, *Mol. Pharmaceutics* **2022**, *19*, 256.